Characterization of temperature and strain fields during cyclic laser shocks

by A. Charbal*,***, L. Vincent ***, F. Hild*, M. Poncelet*, S. Roux* and D. Farcage**

* LMT Cachan, UMR 8535, 61 av. du Président Wilson, F-94235 Cachan cedex, France,
poncelet@ens-cachan.fr, hild@lmt.ens-cachan.fr, stephane.roux@lmt.ens-cachan.fr
** CEA, DEN, DPC, SEARS, F-91191, Gif sur Yvette cedex, France, *daniel.farcage@cea.fr*
***CEA, DEN, DMN, SRMA, F-91191 Gif sur Yvette cedex, France*, ali.charbal@cea.fr, ludovic.vincent@cea.fr*

Abstract

Thermal shocks are applied to a 304L austenitic stainless steel plate with a pulsed laser. A stroboscopic reconstruction is used for IR and visible camera measurements. The displacement fields are measured with regularized Finite Element-Digital Image Correlation (FE-DIC). Different approaches are used to measure the temperature variations (i.e., IR camera and large-band pyrometry). Several ways of determining the emissivity or absorptivity are discussed. The thermal loading is determined by comparing experimental and Finite Element (FE) analyses. An elastoplastic model is then used to compute mechanical fields that are compared with DIC measurements.

1. Introduction

Thermal fatigue occurs in nuclear power plant pipes. The temperature variations are due to the turbulent mixing of fluids that have different temperatures. Many experimental setups have been designed but the measured temperatures have only been punctual and out of the zone of interest (e.g., via thermocouples) [1, 2]. The equivalent strain variation in the crack initiation region is calculated with numerical thermomechanical simulations. In many cases, the comparisons between numerical and experimental results have shown that the crack initiation predictions in thermal fatigue are non-conservative [3]. Some hypotheses, which will not be discussed herein, can be proposed to explain such discrepancies. In this paper, the experimental evaluation of temperature and strain variations is analyzed.

A new testing setup is proposed where thermal shocks are applied with a pulsed laser beam while the thermal and kinematic fields on the specimen surface are measured with infrared (IR) and visible cameras, respectively [4, 5]. Since the usual painted speckles used in Digital Image Correlation (DIC) are not appropriate for the relatively high temperature levels of the tests, a regular grid is created by laser engraving. However, for fatigue studies, this type of pattern is no longer suitable as it does alter the initial surface state of the material. In this case study, only a few cycles are performed and the fatigue aspects (i.e., crack initiation, propagation) are not discussed.

First, experimental tests are performed and different measurement techniques for temperature and kinematic fields are presented. IR camera and pyrometers are used to measure the temperature variation in the zone impacted by the laser beam. To estimate the absolute temperature, the surface emissivities at the respective wavelengths are determined by different methods. The absolute temperature field is then used to apply the actual thermal loading in a decoupled FE model after an identification process of the parameters of the laser beam. Once the thermal loading is generated based upon the experimental data, the stress and strain fields can be computed in the region of interest with an elastoplastic law [6]. The experimental strain variations calculated from the DIC measurements are compared with the predictions obtained with the FE simulation.

2. Experimental Facility and Material

2.1 Experimental Setup

A pulsed laser (TruPulse 156 made by Trumpf, λ = 1064 nm - Fig. 2-1 (1)) is used to apply cyclic thermal shocks to the center of a parallelepiped (Fig. 2-1 (2)). The shock frequency is 2 Hz, the pulse duration is 50 ms and the incident power is equal to 300 W. A focusing optics allows a top-hat power density to be obtained over a disk 5-mm in diameter. Due to a relatively low absorptivity of the polished surface, an inclination of the beam is needed to reflect the incident beam onto a calorimeter (Fig. 2-1 (3)). The calorimeter gives access to the mean power reflected by the sample.

Two fast pyrometers (KGA740-LO made by Kleiber, λ = [1550 nm-2200 nm], Fig. 2-1 (4)) are used to measure, within the impacted zone, the temperature variation on a 2.5-mm central area. Finally, an infrared camera (x6540sc made by FLIR, definition 640 x 512 pixels, λ = [3 μm-5 μm], Fig. 2-1 (5)) is used to measure the change of the thermal field during the laser shocks and a visible camera (MIRO M320S made by Vision Research, definition: 1920 x 1080 pixels, Fig. 2-1 (6)), is used to measure the displacement fields via DIC. Protective filters are used for both IR and visible cameras (Fig. 2-1 (7 and 8)). A 250-W Dedocool spotlight is used to provide the lighting needed for DIC purposes, see Fig. 2-1 (9). The working distance for the IR and visible cameras is 18 cm and 25 cm, respectively. This leads to physical

pixel sizes equal to 60 µm and 12.5 µm, for IR and visible cameras, respectively. The sample is heated up to 400 °C with an electrical resistance whose temperature is controlled by a thermocouple (Fig. 2-1 (10)).

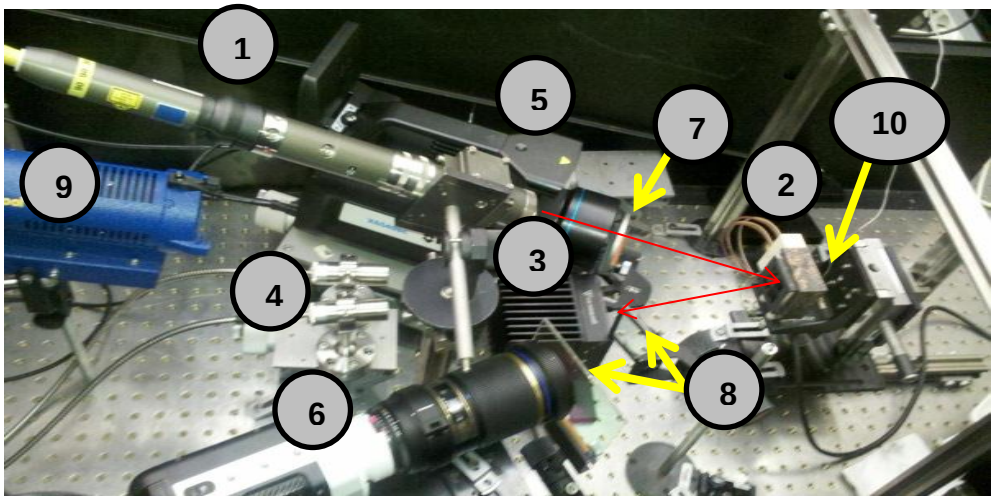

Fig. 2-1: Experimental configuration (see main text for a detailed description of the components labeled in the picture)

2.2 Characterized Sample

The studied sample is a 50×50×10 mm^3 parallelepiped made of 304L austenitic stainless steel. To measure displacement fields by DIC, a regular grid is laser engraved onto an initially polished surface of the sample (Fig.2-2 (a)). The depth of the material affected by the engraving has been estimated to be 4 µm at most (Fig.2-2 (b)). The resulting global emissivity is determined in different ways detailed in Section 3.3.1.

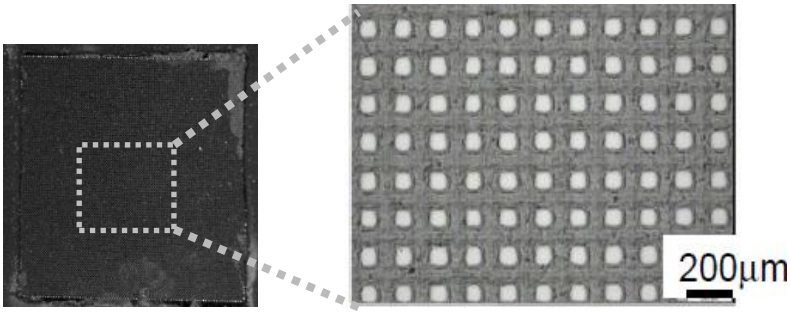

Fig.2-2: *(a) Regular grid laser engraved onto the surface, and (b) a zoom on the periodic pattern*

3. Digital Image Correlation and Infrared Techniques

3.1 Stroboscopic Reconstruction

To measure the displacement and thermal fields at the same time, a stroboscopic acquisition is performed to compensate for the relatively low acquisition frequency of the IR camera compared with the laser shock parameters. The high speed visible camera acquires frames at a much higher rate than the IR camera. Yet, both cameras have been synchronized on the same signal to facilitate the comparison between simulated and experimental fields, in terms of temperature and displacement.

Only four successive thermal shocks acquired at around 180 Hz are used to have a complete thermal shock by stroboscopic reconstruction. This approach provides 34 pictures during one reconstructed pulse, to be compared with only 8 pictures per pulse if no stroboscopic reconstruction were used. During one complete cycle, namely, the increase of temperature and the cooling down phase, the total number of images is 360. To reach a stabilized temperature regime from one pulse to another, approximately 50 cycles have been performed prior to starting the stroboscopic acquisition.

This last aspect was checked with the pyrometer signals acquired continuously at a frequency of 1500 Hz during one hundred cycles.

3.2 Digital Image Correlation

The principle of DIC is to register two images shot at different instants of time, in the present case the reference image f is shot just before the first measured shock and the deformed images g are those acquired during the thermal loading. Most of the time, the main assumption is based upon a gray level conservation between the registered images

$$g(\underline{x} + \underline{u}(\underline{x})) = f(\underline{x}) \tag{1}$$

where f and g are the gray level images, and $\underline{u}(\underline{x})$ the sought displacement field. This conservation equation implies that the two states of the observed surface should be illuminated with the same amount of light. In the global DIC approach used herein, the aim is to minimize the functional over the whole region of interest

$$\tau_{DIC} = \int \left(f(\underline{x}) - g(\underline{x} + \underline{u}(\underline{x}))\right)^2 dx \tag{2}$$

by iteratively correcting the deformed image as $g^n(\underline{x}) = g(\underline{x} + \underline{u}^n(\underline{x}))$ until convergence. The convergence criterion is given by the root mean square (RMS) difference between the displacement at iteration $n+1$ and n, which has to become less than 10^{-6} pixel. The correlation residual is the RMS of the difference between the reference image and the deformed image corrected by the measured displacement field. In the following, regularized FE-DIC is used. The principle consists of discretizing the displacement field with finite elements so that the kinematic unknowns become the nodal displacements [7]. In the present case, 3-noded triangular (T3) elements are chosen. Instead of directly minimizing Eq. (2), the minimization is performed on the total functional τ_t, which consists of the weighted sum of three functionals, namely, one contribution based on gray level conservation, one based on the minimization of the equilibrium gap τ_M, and a last one controlling the displacement fluctuations on the edges of the region of interest τ_B

$$(1 + \omega_M + \omega_B)\tau_t = \tau_{DIC} + \omega_M\,\tau_M + \omega_B\,\tau_B \tag{3}$$

where the weights ω_M and ω_B are proportional to cut-off frequencies of fourth order low-pass (mechanical) filters [8]. In the following analyses, 10-pixel T3 elements are appropriate for the displacement amplitudes to be measured and with the size of the grid pattern. Regularization lengths of 200 pixels for the mechanical and boundary functionals are selected.

3.3 Infrared Techniques

Non-contact temperature measurements are performed using IR pyrometers and an IR camera. First, a calibration procedure is performed, which consists in identifying the transfer function that links the output signal of the device to the temperature of a Black-Body (BB). Second, an accurate determination of the specimen emissivity is needed to transform the measured signal outputs (digital levels) into absolute temperatures.

3.3.1 Emissivity Determination

A first approach to determine the emissivity consists in using a BB with a large emissive surface reflected by the sample surface. The Digital Level (DL) given by the IR camera is computed as [4]

$$DL = \xi DL(T_S) + (1 - \xi)DL(T_{BB}) \tag{4}$$

where T_S is the temperature of the sample, T_{BB} the temperature of the BB, and ξ the emissivity of the specimen. Several temperatures of the BB can be prescribed, ranging from -5 °C to 150 °C, while the temperature of the sample is unchanged. From at least two temperature levels, the global emissivity becomes

$$\xi = 1 - \frac{DL_1 - DL_2}{DL(T_{BB1}) - DL(T_{BB2})} \tag{5}$$

To further increase the sensitivity of the method, more than two values of the BB temperature may be considered.

When the temperature of the sample is much higher than the maximum temperature admissible by the BB (150 °C), the previous approach is no longer applicable. An alternative route consists in depositing a highly emissive black coating on one part of the sample surface near the region of interest. Then by keeping the sample at a known temperature the surface emissivity is estimated as

$$\xi = \frac{DL_{Region\ of\ interest} - DL_{Offset}}{DL_{Black\ painting} - DL_{Offset}} \quad (6)$$

where DL_{Offset} is the digital level representative of the noise of the camera (typically a BB at low temperature or the camera lens cap). If the surface of the sample does not change when its temperature increases (namely, if oxidation is stabilized), then the same value of emissivity should be obtained using either one of the two previous methods. The last one that assesses the luminance of a region of the sample covered by a black painting as a reference is also used with the pyrometers to identify the emissivity in their respective spectral range [1.55 -2.2 μm].

The laser and calorimeter can also provide the emissivity if it is assumed to be equal to the absorptivity (by subtracting the reflected energy measured by the calorimeter from the incident pulse energy). This approach provides the surface emissivity of the surface at the laser wavelength.

3.3.2 Calibration Phases

When IR techniques are to be used, calibration phases on BBs are important to relate the signal outputs of the measuring systems and the sought temperatures. The calibration function used for the large-band pyrometer has the general form of Planck's law, $U = A/(\exp(B/T) - 1)$, where U is the output voltage of the pyrometers and T the absolute temperature of the BB. The calibration then consists of identifying the parameters A and B so that the difference between experimental and predicted output voltages be minimum for 10 values of the BB temperature ranging from 200 °C to 700 °C by steps of 50 °C.

The IR camera was provided with calibration files. However, as the manufacturer performed the calibration at a different working distance (2 meters away from the black body) and settings (no germanium filter) an in-house calibration with the same settings (working distance and germanium filter) as in the experiments has been conducted. It appeared that the reduction of working distance (to 18 cm) was compensated by the introduction of the germanium window resulting in the same outputs was similar to those proposed by the manufacturer.

4. Finite Element Model and Identification of Parameters

To evaluate the complete experimental setup, starting from the estimation of the surface emissivity up to the displacements fields, FE simulations are carried out. These simulations also permit 3D results to be obtained, which are not directly accessible experimentally. Due to symmetry considerations, only one quarter of the sample is modeled to minimize the computation time.

A heat transfer simulation is first performed in which a top-hat heat flux is prescribed on the central zone of the surface. Four parameters are identified in this analysis, namely, the radii of the "top-hat" shape (the experimental temperature profiles show that the edges are not as sharp as the theoretical top-hat) along the Y and Z axes (i.e., ellipsoid shape), the absorption coefficient of the surface and the temperature of the surface just before a laser pulse is emitted. All remaining material parameters are taken from the French design code for nuclear power plants [9]. To compare the measured temperature fields and the FE results, the finite element size in the impacted zone is chosen to be as close as possible to the physical size of the pixels of the IR camera (i.e., 60×60 μm²). As the temperature field is assumed to be symmetric (Fig 4-1 (a)), the latter is averaged as shown in Fig 4-1 (b). By minimizing the difference between the simulated (Fig 4-1 (c)) and measured (Fig 4-1 (d)) temperature fields at the end of a laser pulse, the identification process converges to a set of parameters. The final difference is plotted in Fig 4-1 (e). The residual map is nearly homogenous in some regions and presents very low values. However a ring of higher amplitudes is observed, which is interpreted by the fact that the experimental top-hat is not perfect. Yet, the map is deemed satisfactory.

A thermomechanical simulation is then performed in which the change of the 3D temperature field, which has been previously identified, is prescribed. The mechanical behavior is described by a nonlinear kinematic hardening identified on the results of classical push-pull fatigue tests carried out at 165 and 320 °C. This law has already been used to estimate the strain variations in other thermal fatigue experiments [6]. For the same variations of temperature, the changes of simulated and experimentally measured eigen strains can be compared. It is worth noting that the normal to the sample surface is in the X direction, while the largest size of the impacting laser beam (due to the tilt of the beam) is in the Z direction, the last direction being referred as Y (see Fig 4-1).

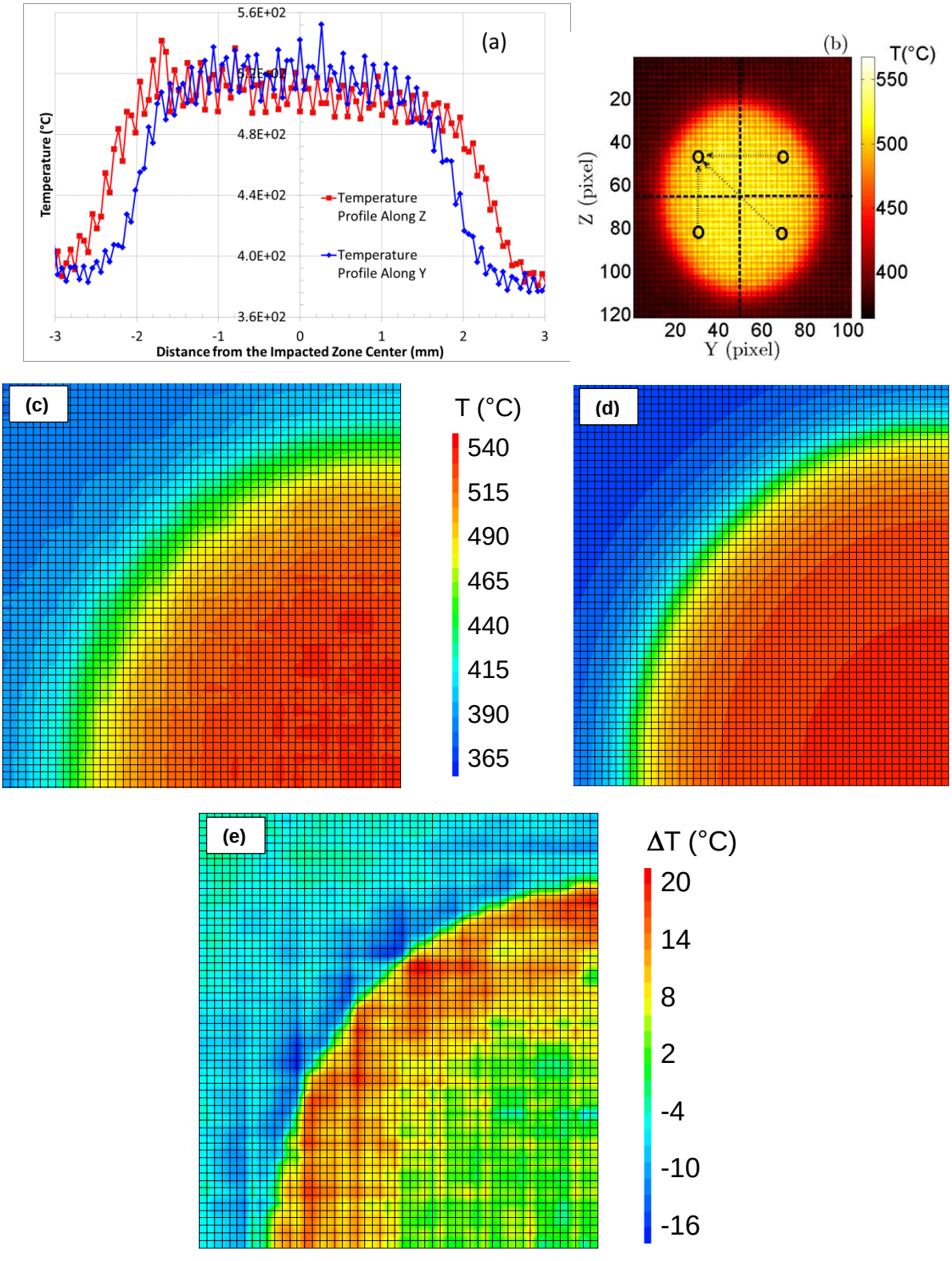

Fig 4-1: *(a) Profiles along Y and Z axes along a row of pixels corresponding to (b) the measured temperature field. (c) Projection of the averaged experimental temperature field and (d) the corresponding field after identification. (e) Residual map representing the difference between the identified and experimental temperature fields (°C)*

5. Results and Discussions

5.1 Experimental and Identified Emissivity and Absorption

Table 5-1 shows the results obtained by the different approaches presented in Section 3.3.1. As expected, the emissivity varies with the wavelength [10]. The following values are obtained: $\varepsilon = 0.68$ with the pyrometers (λ = 1.55-2.2 μm), $\varepsilon = 0.45$ with the IR camera (λ = 3-5 μm) and $\varepsilon = 0.35$ with the calorimeter (λ = 1.064 μm). The important point here is to observe any change in surface emissivity (or absorptivity) when values before and after laser shocks are compared. It is concluded that the same amount of flux is absorbed by the sample and thus a constant loading is applied (it was independently checked using dedicated experiments that the laser did not drift). The identification step provides results that are very close to the experimental ones when the determined absorptivity (0.346 at 540°C) via FE identification is compared with experiments (0.35, see Table 5-1) at the laser wavelength. The size of the hot zone is well approached (Fig. 5-1) since the temperature profiles along both axes are comparable.

Table 5-1: *Emissivity and absorptivity results*

Method	Wavelength (μm)	Sample Temperature Range (°C)	Global Emissivity (Average)
Laser shocks and calorimeter	1.064	20 *and* 300	0.35
Large-band pyrometry	1.55 − 2.2	200 *to* 450	0.68
IR and BB	3 − 5	20	0.43
IR and black painting	3 − 5	200 *to* 450	0.45

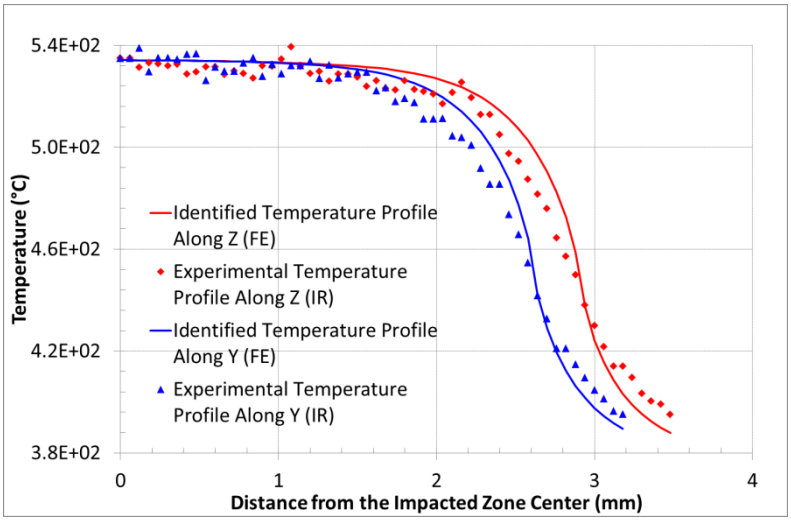

Fig. 5-1: *Experimentally measured (IR) and identified temperature profiles along Z (red) and Y directions (blue)*

5.2 Temperature Measurements

The temperature measured by one pyrometer is then compared in Fig. 5-2 with that obtained with the IR camera. This last measurement is the result of a spatial average over 10 pixels located in the center of the zone impacted by the laser. These last results are similar with a gap of 10 °C at most (e.g., the pyrometers give 550°C while the IR camera 540°C as maximum temperatures). No change in emissivity has been noted in the range 20°C to 400°C, and hence no significant variation is expected when the temperature increases up to 550°C. Therefore, large-band pyrometry and IR camera are expected to be quite reliable for the present experimental conditions. An alternative technique for measuring absolute temperatures was tried based on bichromatic IR pyrometers [11]. The idea was to combine two measurements

performed with a small range of wavelengths (the pyrometers are equipped with narrow filters), close to each other, so that a ratio of intensities for each band provides estimates of the temperature independently of the emittance. Although elegant, this technique was observed to be prone to noise, and a more careful study is to be carried out to make it more reliable for the present experiments.

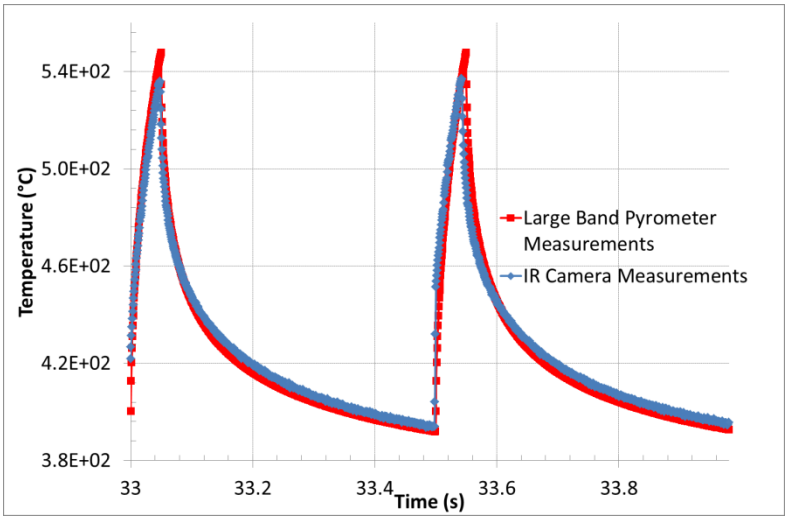

Fig. 5-2: *Temperature history measured by the large-band* pyrometers *and IR thermography*

5.3 Kinematic Fields

As the displacement fields are expected to be small along the Z and Y directions, it is necessary to assist DIC calculations by using a regularized approach. The T3-mesh size is 10 pixels (Fig. 5-3 (a)). The residual errors are small compared with the image dynamic range (since a 12-bit digitization is used, see Fig. 5-3 (b)), namely, the RMS level is equal to 0.6 % of the dynamic range. However, the maximum residuals correspond to the signature of the laser beam. This is due to the fact that the visible camera is sensitive to the flux in the near IR wavelength even behind two hot mirrors. Hence the gray levels are not totally conserved. This effect is only observed on deformed images shot when the laser is on (i.e., not upon cooling down). However, it is believed to have minimal influence on the displacement field measurement as the regularization has been activated.

The measured displacement fields correspond to a 'biaxial' tensile test, (Fig. 5-3 (c and d), in the sense that displacement gradients are observed in both directions. The displacement amplitudes (expressed in pixels) are rather small during thermal loading. The maxima reached along the Y and Z axes are around 0.2 pixel, which is equivalent to 2.5 µm. There is a zone where the displacements are equal to zero on the center of the zone impacted by the laser beam. In-plane strains are then calculated from the measured displacement fields. The comparison between the experimental levels with the FE results focus on the total strain components, which result from thermal expansion and mechanical stresses induced by temperature gradients. The DIC results (Fig. 5-3 (a)) show that the profile of vertical strains ε_{zz} is not symmetric along the Z direction as opposed to that of the horizontal strains ε_{yy}. This presumably results from the fact that the temperature profile along the Z axis is not perfectly symmetric (see Fig 4-1a).

The DIC measurements and the FE results lead to similar spatiotemporal responses, see Fig. 5-4. However, the measured strain levels are higher than those calculated. For instance, the total strain ε_{yy} at the end of the thermal (50-ms) shock in the center of the beam is equal to $7 \cdot 10^{-4}$ with DIC whereas the FE simulations predict a level of $4. \cdot 10^{-4}$. The maximum strain ε_{zz} (for the highest temperature) is measured to be $6 \cdot 10^{-4}$ compared with estimated levels of $3 \cdot 10^{-4}$ (Fig. 5-4 (b)). These discrepancies may be due to poor estimations of the thermal loading, which is related to the emissivity of the surface. They may also be the consequence of the model chosen to describe material behavior, which was identified for temperatures varying between 160 °C and 320 °C (to be compared with levels ranging from 380 °C to 550 °C in the present case). A new identification of the model for the temperature range considered herein is under investigation.

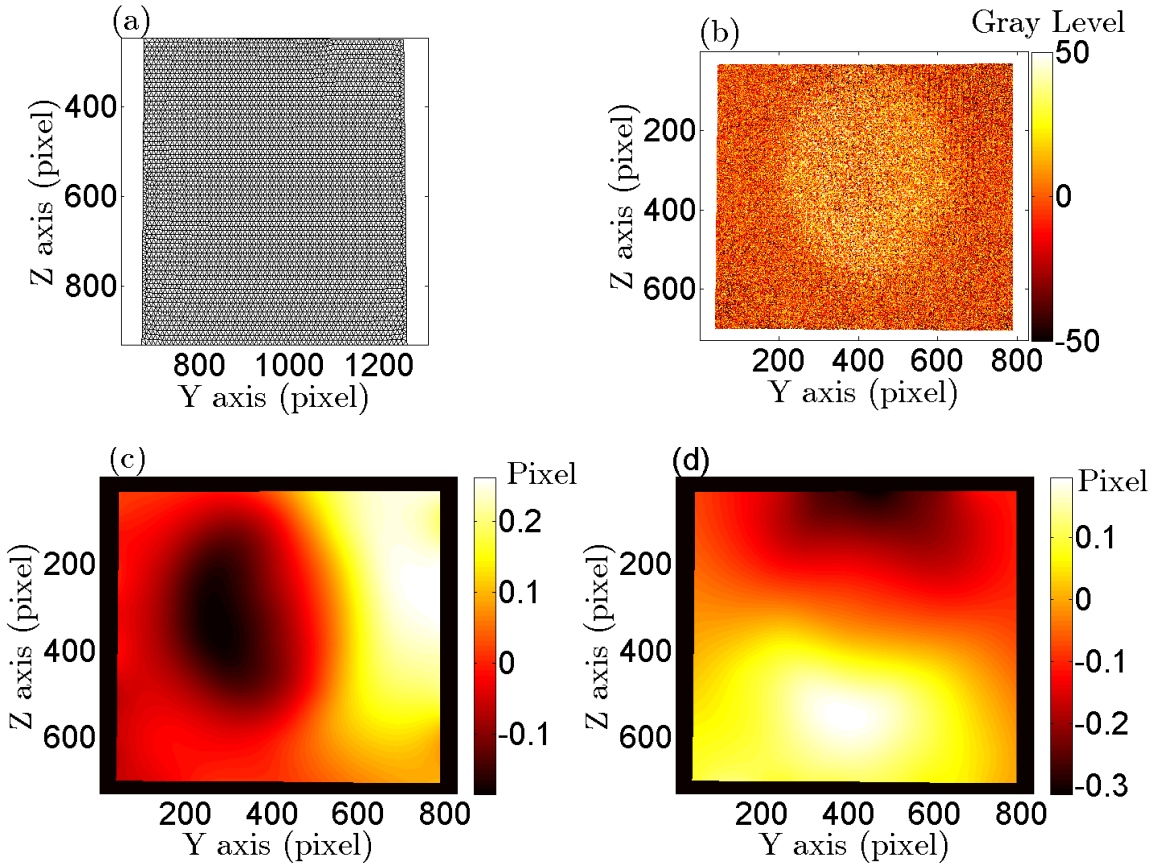

Fig. 5-3: *(a) T3 mesh used in regularized FE-DIC. (b) Correlation residual map (dynamic range of picture: 4080 gray levels). Displacement fields along Y (c) and Z (d) axes*

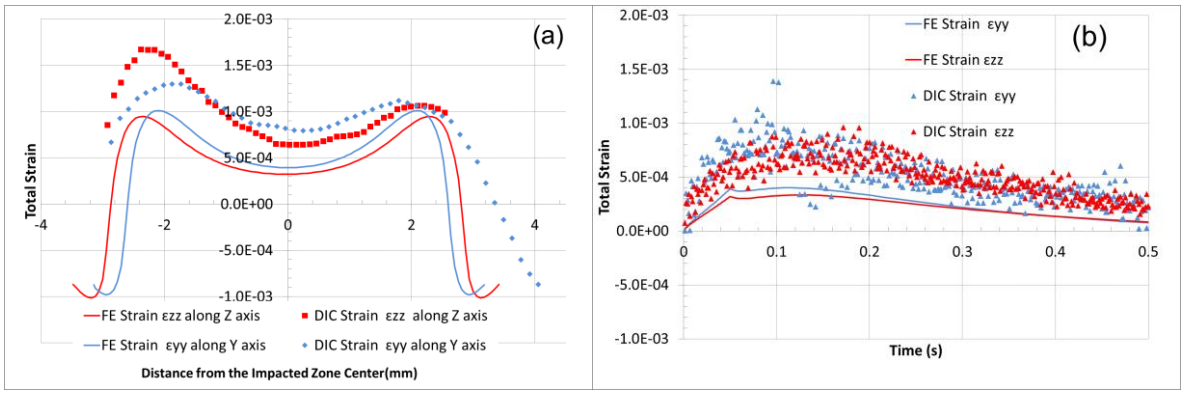

Fig. 5-4: *Total strain comparison between FEM and DIC: (a) at a the end of the shock (50 ms) (b) during one cycle in the center of the impacted zone (stroboscopic reconstruction for DIC)*

In spite of these shortcomings, FE analyses also provide out of plane strains that are not accessible via DIC. Fig. 5-5 shows that the total strain ε_{xx} level is much higher than those calculated (or measured) along the Y and Z directions. This is explained by the fact that along the Y and Z axes the thermal strains (see Fig. 5-5 (a)) are compensated by compressive elastoplastic strains along the Y and Z axes (i.e., mechanical strains), see Fig. 5-5 (b), while no stresses appear in the X direction on the free surface.

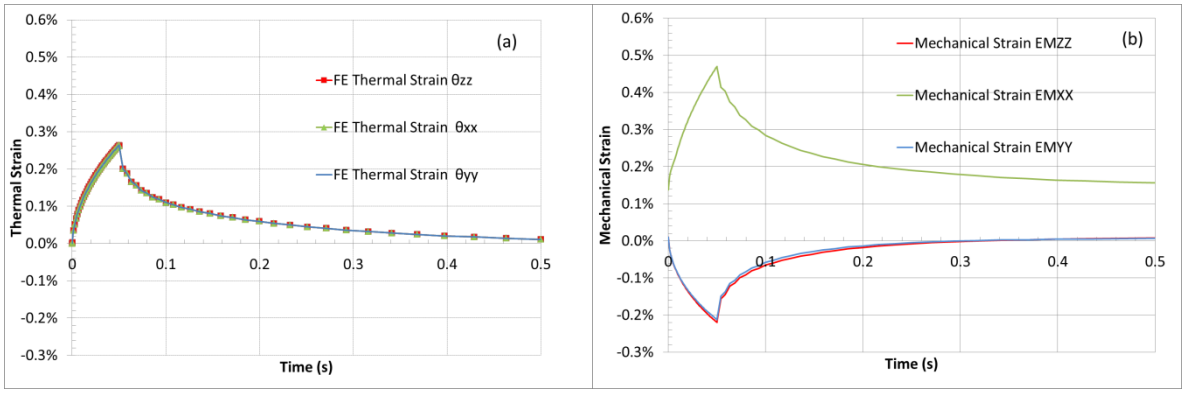

Fig. 5-5: *Predicted contributions to the total strain: (a) thermal strain, (b) mechanical strain*

6. Summary

A new experimental setup using laser shocks has been presented to study thermal fatigue of 304L stainless steel. Experimental techniques providing both thermal and kinematic fields within the loading region have been proposed. Temperature measurements are performed with an IR camera and large-band pyrometers. The results given by both methods are very close. As these methods require the determination of the surface emissivity, different procedures provide estimates for different wavelength ranges.

Once the temperature field is estimated, an identification of the parameters of the laser beam can be carried out in finite element analyses of heat transfer. Parameters such as the absorptivity of the surface are very close to experimental values. This identification step is needed to assess the thermal loading of the analyzed experiment.

The measured strains could then be compared with predicted levels thanks to an elastoplastic simulation. The comparison between the experimental and FE results shows that the constitutive law has to be refined to reduce the small remaining differences between experiment and model. The present study shows that the experimental setup is a very sensitive and discriminating tool to investigate the thermomechanical constitutive law of the tested stainless steel.

Last, thermal fatigue experiments will be carried out in which the in-situ thermal and kinematic fields can be assessed with the proposed experiment. It will then be possible to compare thermal and mechanical fatigue properties of various materials.

REFERENCES

[1] O. Ancelet, S. Chapuliot, G. Henaff and S. Marie, "Development of a test for the analysis of the harmfulness of a 3D thermal fatigue loading in tubes," *International Journal of Fatigue ,* vol. 29, pp. 549-564, 2007.

[2] V. Maillot, A. Fissolo, G. Degallaix and S. Degallaix, "Thermal fatigue crack networks parameters and stability: an experimental study," *International Journal of Solids and Structures ,* vol. 42, pp. 759-769, 2005.

[3] A. Fissolo, S. Amiable, O. Ancelet, F. Mermaz, J. Stelmaszyk, A. Constantinescu, C. Robertson, L. Vincent, V. Maillot and F. Bouchet, "Crack initiation under thermal fatigue: An overview of CEA experience. Part I: Thermal fatigue appears to be more damaging than uniaxial isothermal fatigue," *International Journal of Fatigue ,* vol. 31, pp. 587-600, 2009.

[4] L. Vincent, M. Poncelet, S. Roux, F. Hild and D. Farcage, "Experimental Facility for High Cycle Thermal Fatigue Tests Using Laser Shocks," *Procedia Engineering ,* vol. 66, pp. 669-675, 2013.

[5] C. Esnoul, L. Vincent, M. Poncelet, F. Hild and F. Daniel, "On the use of thermal and kinematic fields to identify strain amplitudes in cyclic laser pulses on AISI 304L strainless steel," *Photomechanics,* 2013.

[6] A. Amiable,S. Chapuilot,S. Contentinescu, A. Fissolo, "A computational lifetime prediction for a thermal shock experiment, Part I: Thermomechanical modeling and lifetime prediction," *Fatigue & Fracture of Engineering Materials & Structures,* Vol. 29, pp 209-217, 2006.

[7] G. Besnard, F. Hild and S. Roux, "Finite-Element Displacement Fields Analysis from Digital Images: Application to Portevin Le Châtelier Bands, Experimental Mechanics, vol. 46, ,pp. 789-803, 2006.

[8] Z. Tomicevic, F. Hild and S. Roux, "Mechanics-aided digital image correlation," *The Journal of Strain Analysis for Engineering Design,* vol. 48, pp. 330-343, 2013.

[9] RCC-M, "Règles de Conception et de Construction des Matériels Mécaniques des Ilots Nucléaires REP," AFCEN, 2009.

[10] G. Gaussorgues, La thermographie infrarouge, 4e ed., Paris: TEC&DOC, 1999.

[11] H. Herne, "The theoretical characteristics of bichromatic pyrometers," *British Journal of Applied Physics,* vol. 4, pp. 374, 1953.